ACS APPLIED MATERIALS & INTERFACES

Research Article

www.acsami.org

Activation and Fluoride-Assisted Phosphating of Aluminum-Silicon-Coated Steel

Paul Schneider,[†] Reinhard Sigel,[‡] Miriam M. Lange,[†] Frank Beier,[§] Frank U. Renner,[†] and Andreas Erbe*,[†]

[†]Max-Planck-Institut für Eisenforschung GmbH, Max-Planck-Strasse 1, 40237 Düsseldorf, Germany
[‡]Physics Department, German University in Cairo, New Cairo City, Egypt
[§]Salzgitter Mannesmann Forschung GmbH, Eisenhüttenstrasse 99, 38239 Salzgitter, Germany

Supporting Information

ABSTRACT: Phosphating is a crucial process in the corrosion protection of metals. Here, activation and fluoride-assisted tricationic phosphating is investigated on aluminum−silicon (AS) coated steel surfaces. Dynamic light scattering results from the activation bath show a bimodal size distribution, with hydrodynamic radii of ~400 nm and ~10 μm. For the smaller particle fraction, static light scattering results are consistent with the interpretation of disklike particles as scattering objects. Particles of the larger fraction sediment with time. In the presence of electrolyte, the scattering intensity from the larger particle fraction increases. Coagulation with time is suggested to be related to the decrease in activity of the activation bath. Scanning Auger microscopy (SAM) shows a higher phosphorus concentration after titanium phosphate activation in the Al-rich areas compared to the Si-rich areas of the AS coatings. There is no correlation between the size of the species in the activation bath, and the size of the phosphate-containing regions on the activated surface. Phosphating was performed in the presence of hexafluorosilicic acid, H_2SiF_6, ammonium hydrogen difluoride, NH_4HF_2, and both, at an initial pH of 2.5. The absence of crystals after phosphating with H_2SiF_6 is an indication that SiF_6^{2-} is the final product of the oxide dissolution in the presence of fluoride. In the presence of NH_4HF_2, the Si-rich regions of the surface are phosphated before the Si-poor (Al-rich) regions. Hence, the phosphate distribution after activation and after phosphating are opposite. These results show that a high surface concentration of phosphate after activation is not sufficient for a high coverage with phosphate crystals after phosphating.

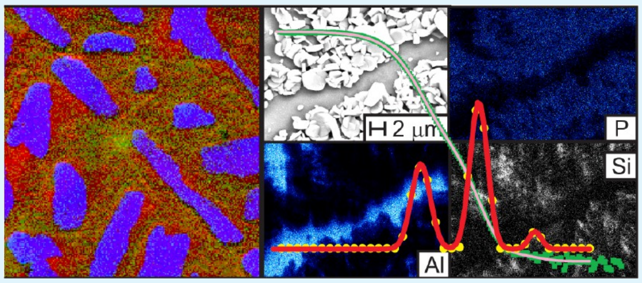

KEYWORDS: *conversion coating, corrosion protection, nucleation, aluminum alloy, crystal growth, colloids*

1. INTRODUCTION

Phosphating is a widely used chemical pretreatment process for metal surfaces, serving purposes in corrosion protection and adhesion promotion for subsequently applied organic coatings.[1,2] Several texts are available to review mechanisms and applications.[3,4] Phosphating furthermore includes a complex sequence of conversion-type reactions, involving an initial corrosion or pickling step, followed by the actual film deposition by a precipitation reaction, which is ideally self-limiting. For such complex processes, simple single-element substrates are often employed to address molecular-level mechanistic understanding.[2] Nevertheless, applications are mostly based on alloys that add complexity such as surface inhomogeneities around precipitates,[5] or new types of reactions (e.g., dealloying[6]). A step in complexity from single-element substrates to more complex but still well-defined substrates is therefore also necessary in fundamental studies.

Historically, surfaces that were phosphated contained predominantly Zn and Fe, i.e., substrates that show pickling under acidic conditions. The pickling is crucial in the establishment of a pH gradient, which leads to a supersaturation of the solution with a phosphate.[7] Local elements play a strong role in the initiation of phosphating.[8] To assist in nucleation of the coatings, titanium phosphates are used in an activation bath prior to phosphating. The properties of the colloidal particles in the activation bath[9,10] and their role in the nucleation of phosphate coatings has been studied,[11] with the interesting result that no traces of the particles from the activation bath were found on the surfaces after activation, but their presence in the bath is crucial for crystal nucleation. Later, the presence of Ti and the presence of particles on activated surfaces was detected.[12−14] More recently, the presence of Ni^{2+} in the phosphating bath in tricationic phosphating was shown to be important in the determination of the location of crystal growth and in the final sealing of the pores between crystals.[15,16] Other investigations study the effect of phosphat-

Received: January 30, 2013
Accepted: April 17, 2013
Published: April 17, 2013

dx.doi.org/10.1021/am400409k | *ACS Appl. Mater. Interfaces* 2013, 5, 4224−4232

ing times and conditions on the mechanical properties,[17] or the effect of temperature on coverage and morphology,[18] on the resulting coatings.

With more complex compositions of alloys and metallic coatings, surfaces may now contain oxides that are not soluble under the acidic conditions present in the phosphating baths, such as Al_2O_3 and SiO_2. In addition, phosphating is also beneficial in the protection of Al alloys. Therefore, the mechanism of phosphate conversion coating formation has been studied on Al.[19] A recent review on phosphate conversion coatings lists the state of the art in this field.[20] The dissolution of a sufficient amount of material from the surface to induce the required pH change near the surface is facilitated by the addition of fluorides in the activation bath, and a tight control of bath composition is crucial for obtaining closed layers.[2] Different fluorides on Al alloys lead to different conversion.[21] The role of the activation has been studied on Al alloys,[13] as have initial stages of the phosphating process itself.[22] Experiments have been performed using a rotating disk electrode to control transport to the interface and to show transport limitation of the phosphating process.[23] Intermetallic particles have been shown to play a role in the phosphate coating formation process on AA 2024.[24,25] Similar situations as on Al occur in phosphating of stainless steels, were an electrochemically assisted phosphating has been used,[26] which is also successfully applied on Fe/Zn substrates.[27,28]

As a model for systems that contain both Si and Al, this work investigates the activation and phosphating of a metallic coating consisting purely of Al and Si. Elemental distribution on an activated surface was obtained by Scanning Auger Microscopy (SAM). To understand the colloidal properties of the activation bath, light scattering is a very suitable technique. However, so far, only very basic data are available,[9] which serves as a motivation for a more thorough light scattering characterization of the activation bath. In subsequent phosphating, the effect of two different fluoride additives, hexafluorosilicic acid (H_2SiF_6) and ammonium hydrogen difluoride (NH_4HF_2), has been investigated.

2. MATERIALS AND METHODS

Substrates from Salzgitter Mannesmann are steels hot-dip-coated with an aluminum silicon (AS) coating. The overall coating thickness is specified to be 10−30 μm. Coating composition is 89−92% Al and ~8−11% Si.[29] The AS coating thickness was found to be 20 μm from a mechanical cross-section. In between AS coating and steel substrate, a 5 μm thick region containing Fe, Al, and Si is found. Substrates were cut to a size of 20 mm × 20 mm. Characterization results of the AS coating before any treatment is shown in the Supporting Information.

Samples were initially cleaned for 10 s in a 0.2 M NaOH solution at 55 °C and rinsed with water (room temperature), before they were put into an activation bath (room temperature, 60 s). The activation bath was the titanium phosphate-based activation Gardolene V6513 from Chemetall, dispersed in water at a concentration of 2 g/L. The actual phosphating bath was a fluoride-free tricationic phosphating bath (Chemetall Gardobond 26T) containing Zn^{2+}, Mn^{2+}, and Ni^{2+} cations. Phosphating was carried out at a temperature of 55 °C for 120 s under constant mechanical stirring of the bath. Phosphating solutions were freshly prepared every morning.

For the investigation of the effect of fluoride additives, NH_4HF_2 (Chemetall Gardobond H 7255) and H_2SiF_6 (Gardobond H 7256) were added to the phosphating bath, to obtain total fluoride concentrations of 1.25 g/L F^- (66 mmol/L F^-) and 0.76 g/L F^- (40 mmol/L F^-), respectively. Consequently, in experiments where both fluorides were combined, the final total F^- concentration was 2.01 g/L (106 mmol/L F^-).

The surface morphology of the samples was studied by field-emission scanning electron microscopy (SEM, ZEISS LEO 1550VP GEMINI). The SEM is coupled to an energy-dispersive X-ray (EDX) spectrometer from Oxford Instruments. For data acquisition and spectra analysis, the software package INCA Energy was used. The crystallography of the samples was studied by X-ray diffraction (XRD) on a Bruker AXS D8 X-ray diffractometer with a Cu−K_α source. A grazing incidence angle (3°) was used for enhancing the diffraction from the surface layer. For peak identification in the diffraction patterns, the Diffrac Plus database JCPDS was used. The powder diffraction files relevant for indexing diffraction patterns in this work were 01−077−1297 for hopeite, 01−085−1327 for aluminum, and 01−075−0589 for silicon. Raman spectra were recorded on a Horiba Jobin Yvon Labram confocal Raman microscope.

Auger electron spectra and Auger microprobe elemental maps were measured by means of a Jeol JAMP-9500F Scanning Auger Microscopy. Using a hemispherical electrostatic energy analyzer (HSA) with a multichannel detector, the measurements were performed in the constant retarding mode with an energy resolution of $dE/E \approx 0.5\%$. Spectra and phosphorus maps were measured at an acceleration voltage of 5 keV and a current of 7 nA, whereas for aluminum and silicon maps, 25 keV acceleration voltage and 10 nA current were used. The measurements were obtained in a UHV system with a base pressure of 1×10^{-9} mbar. Mapping was performed by probing peak and background signal to reduce the influence of topography within the maps. Spectra were analyzed by comparison with reference spectra contained in the instrument control software's own database.

Angular dependent polarized and depolarized dynamic light scattering (DLS) measurements were carried out at the temperature $T = 25$ °C with a helium−neon laser light source (wavelength $\lambda = 633$ nm), an avalanche photo diode detector and a commercial goniometer and correlator (ALV GmbH, Langen, Germany). The directly measured intensity correlation data $g_2(t)$ for different lag times t were transformed to the field correlation function $g_1(t)$ with the standard Siegert relation.[30] The data analysis was based on the regularization program CONTIN,[31,32] which determines the relaxation time distribution $H(\log(t))$ based on $g_1(1)$ data. In this way, also nonexponential $g_1(t)$ data can be treated. Depending on the scattering angle, $H(\log(t))$ was either monomodal or bimodal. A fit with a Gaussian or a sum of two Gaussian functions describes the data well, and allows for each mode the extraction of the average relaxation time τ_C. For further analysis, the scattering angle θ is transformed to the scattering vector magnitude $q = 4\pi n\lambda^{-1}\sin(\theta/2)$, with the solution refractive index n.

For polarized DLS from monodisperse particles under Brownian motion, the θ and λ dependence of τ_C reads $\tau_C^{-1} = Dq^2$ and the translation diffusion constant D can be extracted from DLS data.[30] For polydisperse particle ensembles, it is common to extrapolate the apparent diffusion constant $D_{app} = \tau_C^{-1}q^{-2}$ to $q^2 = 0$, in order to obtain the intensity weighted average of D. The hydrodynamic radius R_h of a particle indicates the radius of a spherical particle with the same D. It is calculated with the Stokes−Einstein relation $D = k_BT/(6\pi\eta R_h)$, where k_B is the Boltzmann constant and η is the solvent viscosity.[30]

In depolarized DLS experiments, a polarizer is placed in front of the detector with an orientation perpendicular to the polarization of the incident laser light. Only particles without spherical symmetry contribute to the depolarized signal. In the simplest case, the θ and λ dependence of τ_C for this geometry becomes $\tau_C^{-1} = Dq^2 + \Theta_R$. Here Θ_R is the constant for rotational diffusion, which has a stronger dependence on the particle size than D. Whereas for small particles and low q, the effect of Θ_R dominates and τ_C^{-1} appears independent of q and θ, τ_C resembles the q^2-dependent translation diffusion behavior of polarized DLS for larger particles.

DLS measurements on the activation solution were challenging, since rather slow variations of the average intensity occurred, which can spoil the measurement of $g_2(t)$. Multiple measurements and averaging were performed to overcome this experimental difficulty. The use of the standard Siegert relation in such a situation might result in a systematic error, which might lead to an overestimation of all

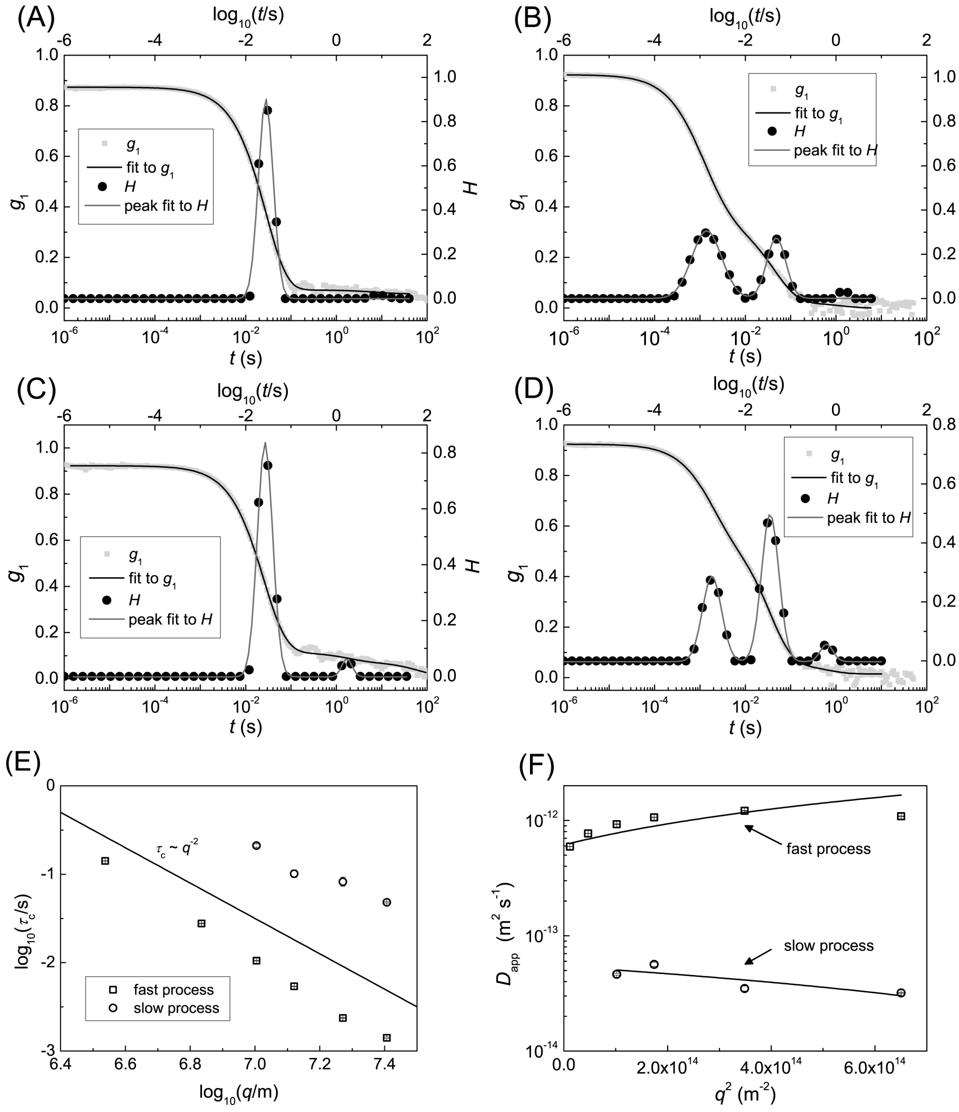

Figure 1. Dynamic light scattering results of freshly prepared activation bath. Field correlation function g_1 and inverted correlation function H of dispersion in pure water at (A) 30 and (B) 150°. After addition of H_3PO_4 at (C) 30 and (D) 150°. (E) Plot of logarithm of relaxation time τ_C as function of the logarithm of the scattering vector q for the two processes. The line represents ideal diffusive behavior. (F) For sample in water, plot of the dependence of the apparent diffusion coefficient D_{app} for the two processes observed, with linear fits to extrapolate to q = 0.

particle sizes by a factor 2. The magnitudes of the changes upon pH change and waiting time within the experiments are beyond the limited accuracy.

Samples for light scattering were prepared by suspending the Gardolene V6513 in water at a concentration of 0.5 g/L, a concentration at the lower limit of specification of the activation. Samples were stirred for 1 h, and then transferred into a light scattering cuvette. To exclude the presence of dust from the preparation, some samples were filtered through a membrane filter of pore diameter 5 μm. To mimic conditions in the phosphating bath, a drop of H_3PO_4 was used to adjust the pH of some of the resulting dispersions to ~2.

3. RESULTS

3.1. Activation. *3.1.1. Light Scattering of Activation Bath.* Results from angle-dependent polarized (VV) dynamic light scattering of the activation bath are shown in Figure 1. The correlation functions (examples are shown in Figure 1 A-D) are dominated by two processes. An analysis of the q-dependence of τ_C (Figure 1E) shows both of them to follow $\tau_C \propto q^{-2}$, typical for diffusive processes.[30] At scattering angles below 120°, the faster process always dominates the overall scattering intensity. Analysis of the q-dependence of the apparent diffusion coefficient D_{app} (Figure 1F) shows for the fast process a significant decrease toward low q, a sign of high polydispersity of the scattering objects. A quantification shows that the faster process is related to the diffusion of particles with R_h of 200–400 nm.

The second, slower diffusive process is becoming more prominent at larger q, as exemplified in the comparison of the inverted correlation functions at scattering angles 30° and 150° in Figure 1. R_h of the species causing the slow process is 5 - 10 μm. This process is also present if the samples had been filtered through membrane filters with a pore diameter of 5 μm prior to experiments. As the particle size of this fraction is larger than the filter pore size, these species must form in solution in an association reaction from the smaller particles.

In addition to the two main processes, some correlation functions show processes with even slower relaxation rate but low overall intensity. These processes may be related to diffusion of bigger particles present at low concentration, or to sedimentation processes, and are also present after filtration of the dispersion prior to experiments. In the systematic analysis, these processes have been discarded.

The sample shows also a signal in depolarized light scattering, which indicates the presence of nonspherical or anisotropic particles. Data analysis shows two relaxation modes slightly faster than for the polarized measurements, plus slower modes which were again discarded. The slight change in relaxation time originates from the effect of rotational diffusion upon the depolarized signal. Due to the big particle size, the rotational diffusion is very slow. The statistical error exceeds of the small magnitude of the relaxation rate τ_C^{-1}, and a closer analysis of the rotational diffusion is not possible.

Experiments in which the p*H* of the dispersion was adjusted to ~2 by addition of H_3PO_4 still show the presence of both diffusive processes with very similar relaxation rate compared to the case in pure water. However, the slower process is gaining intensity compared to the situation in pure water, as shown by a comparison between panels B and D in Figure 1. This result can be understood as an increase in the fraction of larger particles. Particles start to associate or agglomerate because of the screening of electrostatic repulsion with the increasing ionic strength at low pH.

When the same sample is measured more than one day after preparation, the overall scattering intensity is reduced to ~1/5. DLS experiments show that especially the slow process is affected by the decrease. The faster process is still prominently visible in the correlation functions. This result proves that the smaller particle fraction ($R_h \approx 200-400$ nm) is still present after one day, whereas the larger particle fraction has to a large extent sedimented or coagulated. The larger particle fraction is therefore an intermediate in the coagulation progress of the activation colloids.

Further information is gathered from static light scattering (SLS), where the angle dependence of the intensity I of the scattered light is considered. In the double logarithmic plot of Figure 2, a characteristic behavior $I \propto q^{-2}$ is found at low q. The behavior hints to flat scattering particles with a thickness much smaller than λ, so they appear as two-dimensional objects in scattering. Included in Figure 2 as a straight line is a calculated form factor of discs of radius 700 nm.[33] The comparison shows, that the scattering data are compatible with such flat objects, which might be of still larger size. The presence of depolarized light scattering intensity confirms the anisotropic shape of the scattering objects. The intensity is dominated by the fast diffusing particles at low q, so the flat geometry can be assigned to them. The smaller value of R_h detected by DLS is affected by all three dimensions of the particle, especially the small thickness. The larger value of SLS, in contrast, reflects the largest extension in one direction. A detailed fit with an extraction of the radius of gyration as an additional size characterization, is unfortunately not feasible with the data in the small experimental window for q. The deviations at large q can be attributed to the scattering contribution of the larger particles detected by DLS.

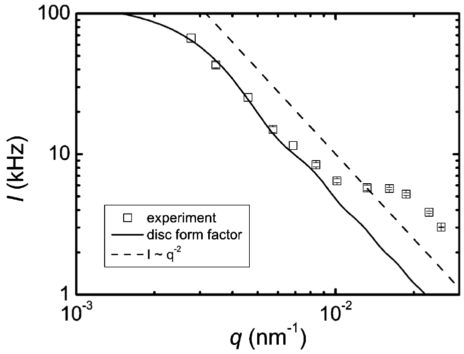

Figure 2. Static light scattering results for activation bath in pure water. Lines: — calculated curve of the form factor of a disc with 700 nm radius, - - - limiting behavior for disk-like particles, $I \propto q^{-2}$.

3.1.2. Activated AS Surfaces. Auger electron spectra of an Si-rich and Si-poor area on an activated AS surface are displayed in Figure 3. The spectra do clearly show the presence of phosphorus in the form of phosphate, especially in the Si-poor areas. As the substrate is phosphate-free, phosphate must originate from the activation treatment. The distribution of the elements is shown in Figure 4, where the ratio of (peak − background) to background signal is plotted. The Si-rich areas contain in general very little phosphate, whereas in the Al-rich

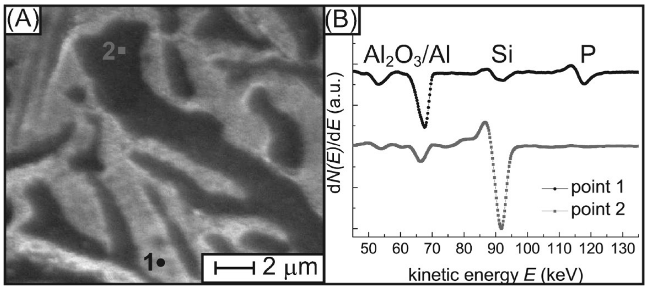

Figure 3. (A) SEM image and (B) Auger electron spectra at the points marked in (A). Peaks in the emission intensity are at ~54 eV (Al^{III}, Al LVV), ~67 eV (Al^0, Al LVV), ~92 eV (Si^0, Si LVV), and ~118 eV (PO_4^{3-}, P LVV). Peak assignment is based on reference spectra supplied with the instrument's software.

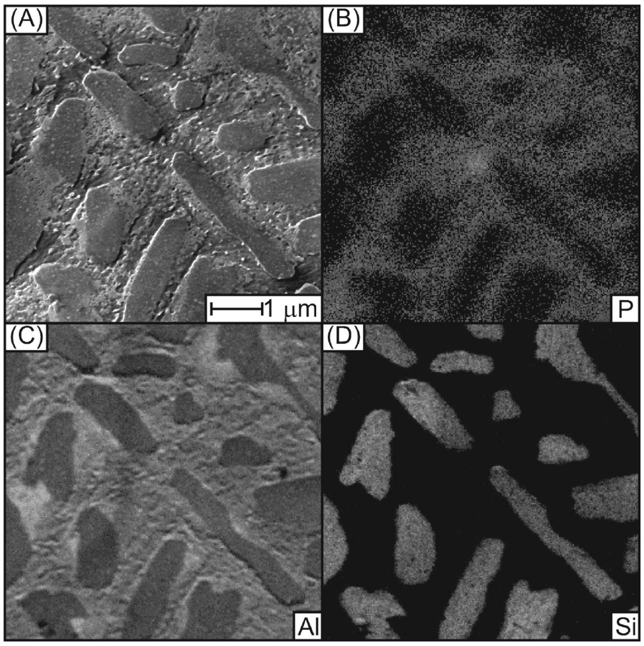

Figure 4. Scanning Auger map of activated AS surface. (A) SE image. Distribution of (B) P, (C) Al, and (D) Si.

areas, the phosphate concentration is substantial. No Ti was detected on these surfaces.

3.2. Phosphating.

Exposing AS samples to the phosphating solution without fluorides, even for hours, does not result in any crystal growth on the surface. After 120 s phosphating time, SE micrographs look almost identical compared to micrographs before exposure to phosphating solution. Images are shown in the Supporting Information.

Two fluorides have been used as bath additives to achieve a dissolution of the oxides covering the surface.

Figure 5a shows an SEM image of a sample exposed to the phosphating solution in the presence of H_2SiF_6. Here, regions with two different characteristics are observed. EDX (Figure 5b) shows only Al peaks in the region, which looks darker and etched. The brighter areas show both Si and Al peaks in EDX. These areas appear more resistant against etching. However, no phosphate crystals grow on either part of the surface.

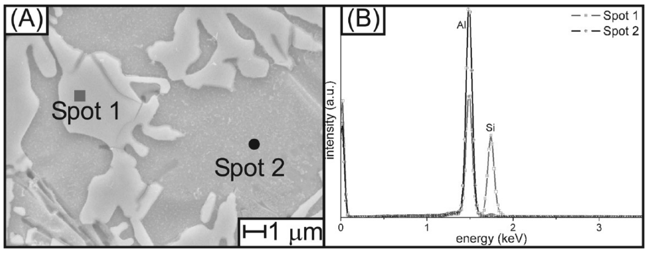

Figure 5. (A) SEM image of a sample treated with H_2SiF_6 as bath additive. (B) EDX patterns of two points on the surface.

Different behavior is observed after addition of NH_4HF_2 to the bath. Figure 6 shows SEM, EDX, spectra and elemental maps. Clearly, crystals are observed on the sample surface, though no complete coverage with crystals is obtained under the experimental conditions (phosphating time, fluoride concentration) used here. The EDX spectrum shows the crystals to consist of Zn, Mn, P, and O, with a low Mn content. Si and Al from the substrate are also observed. The EDX elemental maps shows that the area which is not covered with crystals shows a high content of Al, and no Si content. On the other hand, Si from the substrate is still visible in the areas covered with crystals. This observation shows that phosphate crystals grow in the Si-rich areas, whereas crystal growth is not occurring in Si-poor areas.

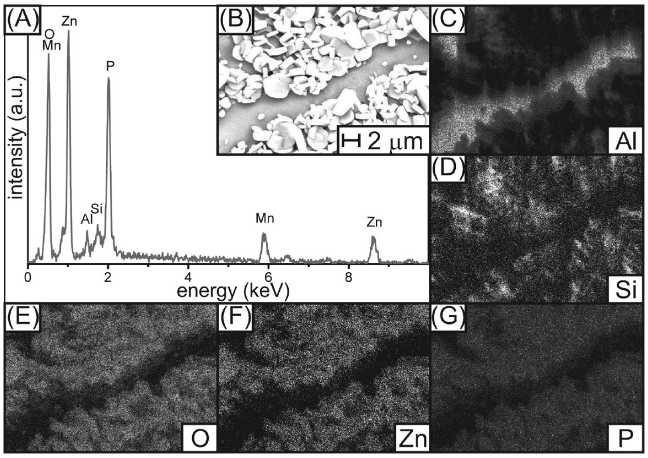

Figure 6. SEM and EDX of a AS sample phosphated in the presence of NH_4HF_2 for 120 s, (A) EDX sum spectrum, (B) SEM, (C−G) elemental map of the element as indicated in the figure.

When phosphating for shorter times than 120 s, surface coverage with crystals is lower than shown in Figure 6, but crystals growth is also restricted to Si-rich areas.

Figure 7 shows XRD patterns and a Raman spectrum of the phosphated surfaces. The XRD pattern shows peaks originating from the substrate, and the two strongest diffraction peaks from hopeite, $Zn_3(PO_4)_2 \cdot 4H_2O$, which is typically observed as product of zinc phosphating in the absence of dissolved Fe^{2+}.[2] The presence of hopeite is confirmed by the presence of peaks at 1057, 997, 940, 594, and 308 cm^{-1} in the Raman spectrum.[34] Furthermore, the peak at 520 cm^{-1} shows the existence of crystalline Si.[35] No hints are observed to the presence of aluminum fluorides, or other phosphates than hopeite.

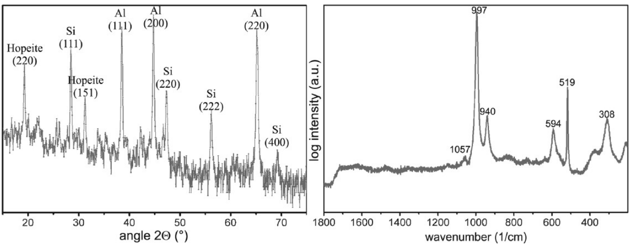

Figure 7. (Left) XRD pattern and (Right) Raman spectrum of an AS-coated steel phosphated in the presence of NH_4HF_2.

When using both fluorides simultaneously, only very few crystals are growing on the surface. An SEM image is shown in the Supporting Information.

4. DISCUSSION

4.1. Activation.

In agreement with previous experiments and general experience,[2,11,13] SEM does not show any particles on the AS coated steel after activation treatment. In a series of landmark works, Van Roy et al. used atomic force microscopy (AFM) and time-of-flight secondary ion mass spectrometry (ToF-SIMS) to detect traces of the activation on surfaces, mainly on AA 5754.[12−14] Using AFM of electropolished samples, particles with a height of 7−8 nm and a lateral extension of 100−300 nm were found on activated surfaces. The appearance of these particles correlated with the observation of Ti and phosphate signals as detected using ToF-SIMS. ToF-SIMS mapping with a lateral resolution of ∼400 nm·400 nm showed individual pixels with high Ti concentration. From the combination of the two observations, the authors identified the particles observed by AFM as particles from the activation bath adsorbed to the surface. SEM micrographs after subsequent phosphating for 2 s lead to the conclusion that the initially deposited nucleation crystals grow initially in a two-dimensional fashion along the surface. The combination of the experimental observations resulted in the proposition of a model of a epitaxial growth of the conversion coating crystals on nucleation crystals.[13]

Light scattering shows the presence of colloidal particles in the activation bath. SAM here shows clearly the presence of phosphate, including its distribution on the surface. The activation is the only source for phosphate. There is, however, in the SAM images no feature that correlates with the particle size determined by DLS. This observation means that the results from this work have to be interpreted in a slightly different way than the interpretation by Van Roy et al..[13] Here, phosphate is likely present as molecular phosphate on the surface. Phosphate has been shown to bind strongly to the γ-Al_2O_3/water interface, with subsequent formation of $AlPO_4$.[36,37] Furthermore, for the thermodynamically unstable γ-Al_2O_3, which initially forms in precipitation processes, the surface has been shown to undergo a transformation when exposed to aqueous solutions.[37,38] A similar mechanism is expected to occur on the ill-defined native oxide on Al. Consequently, the preference of phosphate in the Si-poor regions can be understood because of the affinity of phosphate to Al^{III}. This surface-bound phosphate can either be incorporated into the surface through dissolution from the activation particle and reprecipitation on the surface, or in a direct solid-state reaction between the particles of the activation and the oxide on the substrate.

It is well-known from experience that after ~24 h, the activation bath looses its ability to activate hopeite growth on steel surfaces.[2,11] The DLS experiments show that after 24 h, the fraction with a particle size of several μm is significantly reduced, while the smaller particles are still present in the bath. These results contradict the previous conclusions that for activation, mainly small particles are responsible, which sedimented from the dispersion after 24 h.[10,11] If the presence of a disappearing fraction of particles is responsible for the nucleation effect, the μm-sized particles are candidates to be responsible for activation. Their presence, in the surface region, should, however, easily be detected in SEM after drying, which has not been shown in any experiments, despite attempts here and elsewhere.[11] Therefore, the results obtained here points toward a leaching of phosphate ion species from the activator dispersion into the solution, and redeposition through a precipitation process on the surface. Alternatively, the phosphate may have been incorporated into the surfaces by a direct solid state reaction from particles that were adsorbed to the surface during activation. The fact that the activation dispersion looses its ability to activate nucleation after 24 h may be attributed to a loss in ions available to be incorporated. Combining this information with the size information obtained from DLS, which show that the larger particles sediment with time may be interpreted such that the larger particle fraction is the main source of the ions which are then deposited on the surface. The ion leaching may subsequently lead to a loss in colloidal stability, and the coagulation of the larger particles.

The question remains open to what the active species actually may be that is originating from the particles and released into the activation bath. An analysis of the low-molecular-weight species that are present dissolved in the activation bath may answer this question, but is not a subject of this study.

This interpretation of the results obtained here is different from the interpretation by Van Roy et al., which were obtained for a different surface using different experimental techniques.[13]

4.2. Phosphating. The phosphate layers obtained here are not closed. It is to be expected that a complete surface coverage with phosphate crystals can be achieved with bath optimization, as Al phosphating is applied industrially.[2] Here, instead, we focus on the intermediate stages of the phosphating processes. Using NH_4HF_2 as bath additive, hopeite crystals grow on the AS coated steel surfaces. While phosphate after activation but before phosphating is shown to be higher concentrated in Si-poor areas, after phosphating, the phosphate is mainly concentrated in the Si-rich areas. Consequently, crystal growth either starts in the Si-rich areas. Alternatively, crystal growth may start near the boundaries of Si-poor areas, with a growth direction toward the Si-rich areas. Si-poor areas are not completely phosphated. It can therefore be concluded that high concentration of activation alone is not sufficient for growth of hopeite.

The initial stage in the phosphating is the dissolution of the surface oxides. The net reactions can be written as[39]

$$SiO_2 + 6HF(aq) \rightarrow H_2SiF_6(aq) + 2H_2O \tag{1}$$

and

$$Al_2O_3 + 12HF(aq) \rightarrow 2H_3AlF_6(aq) + 3H_2O \tag{2}$$

The free enthalpies of the two reactions, based on thermodynamic reference data at 25 °C, have been reported as −25 kJ/mol for eq 1 and −17 kJ/mol for eq 2.[39] Dissolution of both oxides is therefore thermodynamically favored in the presence of free fluoride. Comparing the two complexes, these numbers also show that SiF_6^{2-} is thermodynamically more stable than AlF_6^{3-}. Experimental data are available for complex formation constants of the resulting fluoro-complexes. As an example, for the reaction

$$Si(OH)_4(aq) + 6F^-(aq) + 4H^+(aq) \rightleftharpoons SiF_6^{2-}(aq) + 4H_2O \tag{3}$$

an equilibrium constant of $K = [SiF_6^{2-}]/[Si(OH)_4][F^-]^6[H^+]^4 = 1.5 \times 10^{30}$ L^{10} mol^{-10} was determined, using a fluoride electrode.[40] In a potentiometric experiment, the reaction

$$Al^{3+}(aq) + 6F^-(aq) \rightleftharpoons AlF_6^{3-}(aq) \tag{4}$$

was investigated, and equilibrium constants $K = [AlF_6^{3-}]/[Al^{3+}][F^-]^6$ were determined between 3×10^{24} and 1×10^{29} L^6 mol^{-6}, depending on the background salt concentration.[41] These values are significantly higher than the 7×10^{20} L^6 mol^{-6}, which were used by Roberson and Barnes to conclude, after an extensive discussion, that under sufficiently acidic conditions, hexafluorosilicate formation dominates over hexafluoroaluminate formation.[40] Roberson and Barnes also identified pH ~2.5 to be the pH of the highest stability of SiF_6^{2-},[40] a pH near the pH of the phosphating solution. Notice that a direct comparison of the equilibrium constants for eqs 3 and 4 is misleading, because of the different ligands in the initial species.

Mechanistically, AlF_6^{3-} formation is likely to proceed stepwise via mixed fluorohydroxoaluminate or fluoroaquaaluminate complexes.[42] A number of the intermediate complexes have been detected in solutions.[41,42] Although in principle the situation is similar for SiF_6^{2-} formation, only the final product has been reported to be present.[40] An important difference between AlF_6^{3-} formation and SiF_6^{2-} is that (gaseous) SiF_4 was detected as an intermediate in the Si case,[40,43] whereas insoluble AlF_3 is an possible intermediate in the Al case. The latter will redissolve in excess fluoride.

The conclusion from the thermodynamic data available in the literature is clearly that both surface oxides can dissolve under the conditions used in phosphating. Not only can both AlF_6^{3-} and SiF_6^{2-} form under acidic conditions. Even at alkaline pH, the presence of silica has been found to affect the quantitative determination of Al^{III}, because of an effect similar to ion exchangers.[44] A direct application, however, of the experimentally available data to the situation encountered in this work is difficult for three reasons. First, there is little data about the temperature dependence available, which would allow a transfer of the results obtained at room temperature to the temperature of 55 °C in the phosphating bath. Second, the equilibrium constants strongly depend on the background ionic strength.[41] Third, the surface is inhomogeneous, i.e., consists of Si-rich and Si-poor regions. Above these different regions, the equilibrium concentrations of complexes are different. In the course of the ongoing phosphating process, the situation becomes even more complex: H^+ consumption from substrate dissolution leads to a changing pH.

Dissolution kinetics is another factor that is important in the initiation of phosphating. On the one hand, the complex formation equilibrium takes time to establish.[43] On the other hand, tremendous differences have been reported in the dissolution rate of different SiO_2-containing materials in fluoride-containing solutions.[39,45] These have been attributed to the role of defects and disorder in the solids, which offer high energy sites for an attack of the fluoride.[39]

Dissolution kinetics is especially crucial in the second phase of phosphating, when the dissolution of the metal consumes H^+, resulting in a pH gradient, which will eventually lead to the supersaturation of the solution with the layer-forming substance. Changes in pH can strongly affect dissolution kinetics, as for oxides, a catalysis of the dissolution by H^+ has been observed.[46] For a planar, homogeneous interface, the pH and ion concentration as a function of electrode distance in phosphate solutions has been investigated computationally.[47] Experimental investigations with microelectrode techniques have shown good agreement between experiments and calculations in case of controlled electrode reactions.[8] Here, no electrode potential was applied or measured, and no information on currents is available, which is why the pH evolution in the region near the surface cannot be discussed here. Here, with the background presented in the preceding paragraphs, the observation of the resulting surfaces will be taken as starting point for the argumentation.

The first observation is that no phosphating is observed in the presence of SiF_6^{2-} in the concentration used here. The Si-poor surfaces appear strongly etched, while the Si-rich surface appears not attacked, compared to exposure to the phosphating solution without any fluoride. The lack of etching on the Si-rich surfaces can be understood, as SiF_6^{2-} is supposed to be the final product of SiO_2 dissolution under the conditions present here. Hexafluorosilicic acid is well-known not to etch glass.[48] On the other hand, SiF_6^{2-} etches Al-rich (Si-poor) regions of the surface. The etching can be understood, as a certain equilibrium concentration of AlF_6^{3-} is developing. However, no hopeite growth is observed in the etched regions. Obviously, the dissolution speed of Al with concurrent hydrogen evolution is not sufficient to produce a high pH near the surface to trigger hopeite precipitation. Besides a too low dissolution rate, the aforementioned (section Section 4.1) phosphate adsorption and $AlPO_4$ formation may hinder the dissolution. No evidence is found for precipitation of insoluble fluorides (AlF_3, AlF_6^{3-} salts) here, though AlF_3 formation has been shown to occur in initial stages of the phosphating of AA 2024,[24] and the precipitation of Na_3AlF_6 has been systematically studied on AA 1050.[23]

The second observation is that in the presence of NH_4HF_2 in the bath, formation of hopeite is occurring predominantly in Si-rich regions of the surface, whereas Si-poor regions are covered later. For the interpretation of this fact, we need to consider the behavior of the oxide-free substrate in the presence of fluoride, as the above-mentioned thermodynamic analysis shows that fluoride can dissolve both the oxides of Si and Al under acidic conditions. As the AS coatings are prepared from a melt, the resulting solid semiconductor/metal interface is likely to be an Ohmic contact, as there is sufficient possibility for interdiffusion of the two components into the respective other one. Considering the active dissolution of the substrate components (provided there is no layer hindering dissolution on either material) is a typical situation as encountered in corrosion of two materials in galvanic contact, which may result in cathodic protection of the nobler component. The standard electrode potentials $E^{\ominus}$ at 25 °C are for

$$AlF_6^{3-} + 3e^- \rightleftharpoons Al + 6F^- \quad E^{\ominus} = -2.069\ \mathrm{V} \tag{5}$$

and for

$$SiF_6^{2-} + 4e^- \rightleftharpoons Si + 6F^- \quad E^{\ominus} = -1.24\ \mathrm{V} \tag{6}$$

(see ref 49).

Both potentials are well in the region were the individual materials should dissolve under H_2 evolution. Obviously, Si is the nobler component, which means that Al should dissolve preferentially. As dissolution with concurrent H_2 evolution leads to the pH increase needed for hopeite precipitation, hopeite should precipitate on Si-poor regions, as opposed to the observations in this work. This observation is, however, consistent with the interpretation that SiF_6^{2-} is the most stable final product of fluoride etching. Dissolution is then basically limited by the availability of fluorides, and etching is occurring faster in the Si-rich areas, inducing hopeite growth. The Si etching may consume most of the available free F^-, leading to insufficient supply for the etching of the Al-rich surface.

The third observation is the effective suppression of hopeite formation in the presence of both fluorides. Adding the final product of the SiO_2 dissolution leads to suppression of dissolution at the same concentration of free F^-. This observation is therefore also consistent with the explanation that SiF_6^{2-} is the most stable species in the solution under the conditions used in this work.

The results presented here differ from results of the phosphating of Al alloys at pH ~4.5, where SiF_6^{2-} has been found to yield layers with larger weight than NH_4HF_2.[21] These differences are consistent with the reported higher stability of SiF_6^{2-} at lower pH.[40] An important difference to Al alloys investigated in the literature is the lack of intermetallic particles in the AS coatings. The presence of intermetallic particles has been shown to substantially affect the mechanism of phosphating of Al alloys.[22,25] A further source of differences are different convection speeds, which lead to different transport speeds of species toward and from the surface: both oxide dissolution,[50] as well as phosphate precipitation,[23] have been shown to be severely affected by transport. Thus, layer morphologies obtained in different geometries may differ substantially.

5. CONCLUSION

Although there is general consensus that for phosphating of Al-alloys, a thorough control of the bath composition is needed,[2] bath control becomes even more critical in the case of surfaces which contain Si and Al. This work finds that in this case, the phosphate layers over the Si-rich areas are closed first.

Light scattering data of the activation bath is consistent with the presence of disklike particles. The data clearly shows a bimodal size distribution, from which the larger particle fraction disappears with time. This disappearance correlates with the loss of the activation ability of the bath. After exposure of the AS surfaces to the activation bath, phosphate is found predominantly in Si-poor, i.e., Al-rich regions of the surface. The extension of the phosphate-rich regions correlates with the Al-presence on the substrate surface, but there is no correlation to the size observed in light scattering. The phosphate found on the substrate surface is suggested to be leached from particles of the activation bath. Alternatively, phosphate may be incorporated into the surface as a result of a direct exchange reaction between surface and the activation particles.

The results for the activation obtained here differ from the results obtained on Mg-rich Al alloy AA 5754, were particles observed in AFM have been connected to the appearance of Ti signals in ToF-SIMS.[12−14] These differences may be related to different behavior of the activation on the different surfaces (Mg-rich vs Si-rich). From the work conducted here, it is also not clear if the phosphate observed here is the phosphate that is responsible for crystal nucleation. In the works by Van Roy et al. the concentration of Ti correlates well with the ability to nucleate crystals,[12−14] which may imply that Ti is a better indicator of the nucleation sites than phosphate.

In this work, the presence of NH_4HF_2 was crucial for the observation of a significant number of crystals on the AS surfaces. This observation contrasts the situation in the work of Van Roy, where no mention is made of the presence of fluorides in the phosphating bath.[13] The fluoride-induced surface etching here obviously predominantly happens in the Si-rich areas. The preference of phosphating of Si-rich areas is explained by the role of fluorides in the phosphating process, as SiF_6^{2-} is forming as a stable product of the Si dissolution. For this reason, at the pH ~2.5 used here, the addition of SiF_6^{2-} effectively suppresses phosphating, in contrast to behavior at higher pH.[21]

While the role of phosphating in industrial processes is likely to dwindle in the coming years, due to its large environmental impact, the complex colloid, surface, and possible solution chemistry during activation and initial stages of the growth process still presents a number of challenges.

■ ASSOCIATED CONTENT

Ⓢ Supporting Information

Characterization of substrate surfaces, surface after exposure to phosphating solution without fluoride, and surface after exposure to phosphating solution containing both NH_4HF_2 and H_2SiF_6. This material is available free of charge via the Internet at http://pubs.acs.org.

■ AUTHOR INFORMATION

Corresponding Author

*E-mail: a.erbe@mpie.de or aerbe@arcor.de.

Notes

The authors declare no competing financial interest.

■ ACKNOWLEDGMENTS

P.S. thanks Salzgitter Mannesmann Forschung GmbH (SZMF) for a scholarship in the frame of the International Max Planck Research School for Surface and Interface Engineering in Advanced Materials (IMPRS-SurMat). M.M.L. thanks SZMF for a collaborative research project. The authors thank Prof. M. Stratmann for continuous support and Andreas Wieck for fruitful discussions.

■ REFERENCES

(1) Freeman, D. *Phosphating and Metal Pretreatment*; Woodhead-Faulkner: Cambridge, U.K., 1986; pp 9−120.

(2) Rausch, W. *Die Phosphatierung von Metallen*, 3rd ed.; Eugen, G., Ed.; Leuze Verlag: Bad Saulgau, Germany, 2005; pp 15−272.

(3) Ogle, K.; Buchheit, R. G. In *Encyclopedia of Electrochemistry*; Bard, A., Stratmann, F. G., M., Eds.; Wiley-VCH: Weinheim, Germany, 2007; Vol. *4*, Chapter Conversion Coatings, pp 460−499.

(4) Narayanan, T. S. *Rev. Adv. Mater. Sci.* **2005**, *9*, 130−177.

(5) Kappes, M.; Kovarik, L.; Mills, M. J.; Frankel, G. S.; Miller, M. K. *J. Electrochem. Soc.* **2008**, *155*, C437−C443.

(6) Pareek, A.; Borodin, S.; Bashir, A.; Ankah, G. N.; Keil, P.; Eckstein, G. A.; Rohwerder, M.; Stratmann, M.; Gründer, Y.; Renner, F. U. *J. Am. Chem. Soc.* **2011**, *133*, 18264−18271.

(7) Ghali, E. I.; Potvin, R. *Corros. Sci.* **1972**, *12*, 583−594.

(8) Klusmann, E.; Schultze, J. *Electrochim. Acta* **1997**, *42*, 3123−3134.

(9) Tegehall, P.-E. *Colloids Surf.* **1989**, *42*, 155−164.

(10) Tegehall, P.-E. *Colloids Surf.* **1990**, *49*, 373−383.

(11) Tegehall, P.-E.; Vannerberg, N.-G. *Corros. Sci.* **1991**, *32*, 635−652.

(12) Van Roy, I.; Van den Broeck, I.; Terryn, H.; Goeminne, G.; Poleunis, C.; Bertrand, P.; Delplancke, M. In *ECASIA 97: 7th European Conference on Applications of Surface and Interface Analysis*; Olefjord, I., Nyborg, L., Briggs, D., Eds.; John Wiley & Sons: Chichester, U.K., 1997; pp 995−998.

(13) Van Roy, I.; Terryn, H.; Goeminne, G. *Colloids Surf., A* **1998**, *136*, 89−96.

(14) Van Roy, I.; Terryn, H.; Goeminne, G. *Trans. Inst. Met. Finish* **1998**, *76*, 19−23.

(15) Zimmermann, D.; Muñoz, A.; Schultze, J. *Electrochim. Acta* **2003**, *48*, 3267−3277.

(16) Zimmermann, D.; Muñoz, A.; Schultze, J. *Surf. Coat. Technol.* **2005**, *197*, 260−269.

(17) Kumar, A.; Bhola, S.; Majumdar, J. D. *Surf. Coat. Technol.* **2012**, *206*, 3693−3699.

(18) Popić, J.; Jegdić, B.; Bajat, J.; Veljović, Đ.; Stevanović, S.; Mišković-Stanković, V. *Appl. Surf. Sci.* **2011**, *257*, 10855−10862.

(19) Cheng, B.; Ramamurthy, S.; McIntyre, N. *J. Mater. Eng. Perform.* **1997**, *6*, 405−412.

(20) Kulinich, S.; Akhtar, A. *Russ. J. Non-Ferrous Met.* **2012**, *53*, 176−203.

(21) Burokas, V.; Martušienė, A.; Girčienė, O. *Surf. Coat. Technol.* **2007**, *202*, 239−245.

(22) Susac, D.; Sun, X.; Li, R.; Wong, K.; Wong, P.; Mitchell, K.; Champaneria, R. *Appl. Surf. Sci.* **2004**, *239*, 45−59.

(23) Buytaert, G.; Terryn, H.; Hubin, A. *Trans. Inst. Met. Finish.* **2002**, *80*, 142−146.

(24) Akhtar, A.; Wong, K.; Mitchell, K. *Appl. Surf. Sci.* **2006**, *253*, 493−501.

(25) Akhtar, A.; Susac, D.; Wong, P.; Mitchell, K. *Appl. Surf. Sci.* **2006**, *253*, 502−509.

(26) Oskuie, A.; Afshar, A.; Hasannejad, H. *Surf. Coat. Technol.* **2010**, *205*, 2302−2306.

(27) Kellner, F. J. J.; Schütze, K.; Kreutz, C.; Virtanen, S. *Surf. Interface Anal.* **2009**, *41*, 911−917.

(28) Jegannathan, S.; Arumugam, T.; Narayanan, T. S.; Ravichandran, K. *Prog. Org. Coat.* **2009**, *65*, 229−236.

(29) *Charakteristische Merkmale 09−Schmelztauchveredeltes Band und Blech*; Stahl-Informations-Zentrum: Düsseldorf, Germany, 2005; p 17.

(30) Berne, B. J.; Pecora, R. *Dynamic Light Scattering. With Applications to Chemistry, Biology, and Physics*; Dover Publications: Mineola, NY, 2000.

(31) Provencher, S. *Comput. Phys. Commun.* **1982**, *27*, 213−227.

(32) Provencher, S. *Comput. Phys. Commun.* **1982**, *27*, 229−242.

(33) Higgins, J.; Benoit, H. *Polymers and Neutron Scattering*; Clarendon: Oxford, 1994; p 156.

(34) Pawlig, O.; Schellenschläger, V.; Lutz, H.; Trettin, R. *Spectrochim. Acta, Part A* **2001**, *57*, 581−590.
(35) Parker, J. H.; Feldman, D. W.; Ashkin, M. *Phys. Rev.* **1967**, *155*, 712−714.
(36) Laiti, E.; Persson, P.; Öhman, L.-O. *Langmuir* **1996**, *12*, 2969−2975.
(37) Laiti, E.; Persson, P.; Öhman, L.-O. *Langmuir* **1998**, *14*, 825−831.
(38) Lefèvre, G.; Duc, M.; Lepeut, P.; Caplain, R.; Fédoroff, M. *Langmuir* **2002**, *18*, 7530−7537.
(39) Mikeska, K. R.; Bennison, S. J. *J. Am. Ceram. Soc.* **1999**, *82*, 3561−3566.
(40) Roberson, C.; Barnes, R. B. *Chem. Geol.* **1978**, *21*, 239−256.
(41) Corbillon, M.; Olazabal, M.; Madariaga, J. *J. Solut. Chem.* **2008**, *37*, 567−579.
(42) Lisbona, D. F.; Steel, K. M. *Sep. Purif. Technol.* **2008**, *61*, 182−192.
(43) Urbansky, E. T.; Schock, M. R. *Int. J. Environ. Stud.* **2000**, *57*, 597−637.
(44) Tomcsanyi, L.; Lanyi, G. *Anal. Chim. Acta* **1972**, *62*, 377−384.
(45) Knotter, D. M. *J. Am. Chem. Soc.* **2000**, *122*, 4345−4351.
(46) Kline, W.; Fogler, H. *J. Colloid Interface Sci.* **1981**, *82*, 93−102.
(47) Auinger, M.; Katsounaros, I.; Meier, J. C.; Klemm, S. O.; Biedermann, P. U.; Topalov, A. A.; Rohwerder, M.; Mayrhofer, K. J. J. *Phys. Chem. Chem. Phys.* **2011**, *13*, 16384−16394.
(48) Wiberg, N. *Hollemann-Wiberg−Lehrbuch der Anorganischen Chemie*, 101st ed.; Walter de Gruyter: Berlin, 1995; p 907.
(49) Vanýsek, P. In *CRC Handbook of Chemistry and Physics*, 93rd ed. (Internet Version 2013); Haynes, W., Ed.; CRC Press/Taylor and Francis: Boca Raton, FL, 2013; Chapter Electrochemical Series, pp 5−80−5−89.
(50) Žutić, V.; Stumm, W. *Geochim. Cosmochim. Acta* **1984**, *48*, 1493−1503.